

## Explicit Forecasts of Winter Precipitation Using an Improved Bulk Microphysics Scheme. Part II: Implementation of a New Snow Parameterization

GREGORY THOMPSON, PAUL R. FIELD, ROY M. RASMUSSEN, AND WILLIAM D. HALL

*National Center for Atmospheric Research,\* Boulder, Colorado*

(Manuscript received 20 September 2007, in final form 19 March 2008)

### ABSTRACT

A new bulk microphysical parameterization (BMP) has been developed for use with the Weather Research and Forecasting (WRF) Model or other mesoscale models. As compared with earlier single-moment BMPs, the new scheme incorporates a large number of improvements to both physical processes and computer coding, and it employs many techniques found in far more sophisticated spectral/bin schemes using lookup tables. Unlike any other BMP, the assumed snow size distribution depends on both ice water content and temperature and is represented as a sum of exponential and gamma distributions. Furthermore, snow assumes a nonspherical shape with a bulk density that varies inversely with diameter as found in observations and in contrast to nearly all other BMPs that assume spherical snow with constant density. The new scheme's snow category was readily modified to match previous research in sensitivity experiments designed to test the sphericity and distribution shape characteristics. From analysis of four idealized sensitivity experiments, it was determined that the sphericity and constant density assumptions play a major role in producing supercooled liquid water whereas the assumed distribution shape plays a lesser, but nonnegligible, role. Further testing using numerous case studies and comparing model results with in situ and other observations confirmed the results of the idealized experiments and are briefly mentioned herein, but more detailed, microphysical comparisons with observations are found in a companion paper in this series (Part III, forthcoming).

### 1. Introduction

A new bulk microphysical parameterization (BMP) has been developed for the Weather Research and Forecasting (WRF) Model, the fifth-generation Pennsylvania State University–National Center for Atmospheric Research Mesoscale Model (MM5), and other mesoscale models. Most existing BMPs in WRF/MM5 are based on the Lin et al. (1983) scheme; however, the new scheme incorporates a large number of improvements to both physical processes and computer coding. The new scheme explicitly predicts the mixing ratios of five liquid and ice species: cloud water, rain, cloud ice, snow, and graupel. In addition, the number concentration of cloud ice is predicted. As such, it is a single-moment scheme with the exception of the double-moment cloud ice variable. While full double-moment

schemes are rapidly becoming available in numerical models (Morrison and Pinto 2005; Milbrandt and Yau 2005; Seifert and Beheng 2006; Meyers et al. 1997), their increased cost due to the prediction of a second moment (number concentration in most cases) deters from their use in real-time numerical weather prediction. In designing this new scheme, the objectives were: 1) to improve quantitative precipitation forecasts (QPFs), 2) to improve forecasts of water phase at the surface and aloft (in particular to support aviation applications to forecast aircraft icing), 3) to incorporate recent microphysical observations from various field projects, and 4) to fulfill the requirements of real-time modeling needs in terms of speed.

Rather than continue to make relatively small strides in improving decades-old, legacy microphysical schemes (cf. Reisner et al. 1998; Thompson et al. 2004; Hong et al. 2004), our approach was to scrutinize the flaws of most single-moment schemes and improve various physical assumptions to force the new scheme to act more like a full double-moment (or higher order) scheme. In fact, as often as possible, the new scheme employs techniques generally found only in spectral/bin microphysical schemes through the use of lookup

---

\* The National Center for Atmospheric Research is sponsored by the National Science Foundation.

---

Corresponding author address: Gregory Thompson, NCAR–RAP, P.O. Box 3000, Boulder, CO 80301-3000.  
E-mail: gthompson@ucar.edu

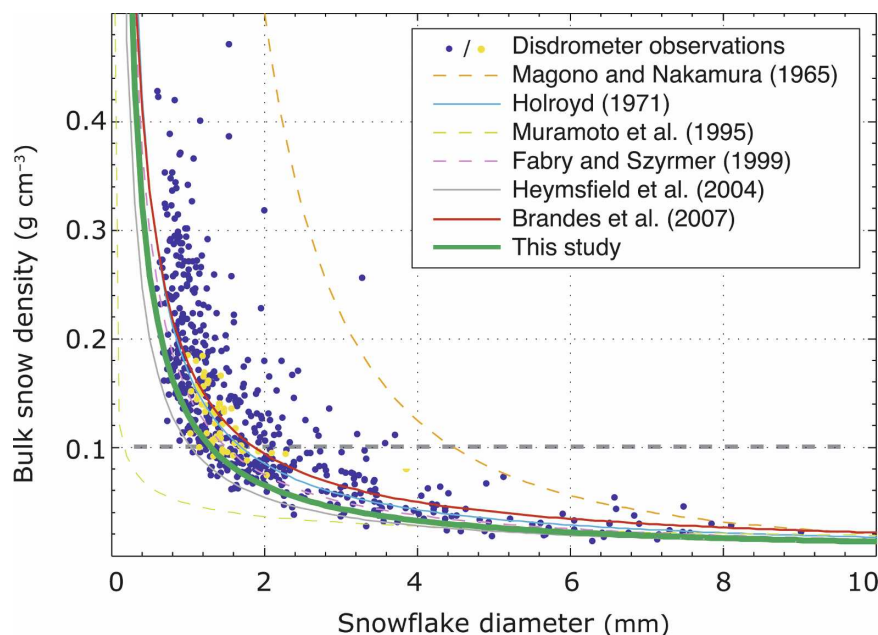


FIG. 1. Plot of bulk snow particle density vs diameter showing disdrometer observations of Brandes et al. (2007) and the modeled relationship using assumptions in the new bulk microphysics scheme. The typical value used in most models is a constant ( $0.1 \text{ g cm}^{-3}$ ).

tables. However, the lack of observations and scientific knowledge (ice initiation, hydrometeor collection, vapor depositional growth, etc.) remain for some processes so the new BMP is regularly compared against results using the bin models of Geresdi (1998) and Lynn et al. (2005) plus the double-moment BMPs of Morrison and Pinto (2005) and Seifert and Beheng (2006) as well as against observations.

In this paper, the details of a new snow parameterization are described in section 2, whereas the remaining aspects of the new bulk scheme are briefly mentioned next and fully detailed in appendix A. New features specific to this version of the bulk scheme compared to that described in Thompson et al. (2004, hereafter Part I) description include

- a generalized gamma distribution shape for each hydrometeor species;
- a y intercept of rain that depends on the rain mixing ratio and whether an apparent source is melted ice;
- a y intercept of graupel that depends on the graupel mixing ratio;
- a more accurate saturation adjustment scheme;
- a variable gamma distribution shape parameter for cloud water droplets based on observations;
- a lookup table for freezing of water drops;
- a lookup table for transferring cloud ice into the snow category;
- improved vapor deposition, sublimation, and evaporation;

- variable collection efficiency for rain-, snow-, and graupel-collecting cloud droplets; and
- improved rain-collecting snow and graupel.

Results of idealized, two-dimensional sensitivity experiments replicating and testing previous snow assumptions are found in section 3. The ramifications of these experiments are summarized in section 4, including a discussion of the same sensitivity experiments applied to a three-dimensional case study. Future papers in this series will contain more detailed comparisons of modeled versus observed hydrometeors for both cool and warm season events.

## 2. Snow distribution assumptions

Most BMPs assume spherical snow with constant bulk density (cf. Lin et al. 1983; Reisner et al. 1998; Hong et al. 2004; Thompson et al. 2004; and others) whereas numerous observational studies over decades clearly demonstrate that its density varies inversely with size (see Fig. 1). In practice, the spherical and constant-density snow assumption is applied in models through the assumed mass–diameter relation, usually with the power law:  $m(D) = (\pi/6)\rho_s D^3$ , where  $\rho_s$  is the assumed bulk snow density and  $D$  is particle diameter. Observational studies of snow at the surface and aloft rarely support this assumption, instead finding the ex-

ponent is closer to 2 than to 3 (e.g., Westbrook et al. 2004; Brandes et al. 2007; Mitchell et al. 1990). One of the earliest modeling studies to deviate from spherical snow appears to be Cox (1988), who used the relation  $m(D) = 0.069D^2$ , which we adopted for use in the new bulk scheme. As such, the new scheme considers snow to be primarily composed of fractal-like aggregated crystals, which likely captures the vast majority of the actual snow mass reaching the earth's surface. A more sophisticated snow habit treatment has been recently incorporated into a microphysics scheme (Woods et al. 2007) following the individual habit classifications of Locatelli and Hobbs (1974), but this has not been shown to improve QPFs beyond the much simpler relation used herein and is more computationally prohibitive.

Another, nearly universal model assumption is the use of an exponential shape for the snow size distribution:  $N(D) = N_0 e^{-\lambda D}$ , where  $N_0$  is the  $y$ -intercept parameter and  $\lambda$  is the slope of the distribution. Even models that are coded to represent the distribution in a generalized gamma form [e.g., Eq. (A1)] are typically applied with the shape parameter set to zero, thus reverting to exponential form. Choosing  $N_0$  remains problematic for any BMP whether constant, as it was in the original formulation by Lin et al. (1983), or variable, as it was in Reisner et al. (1998) and Part I. Field et al. (2005) analyzed 9000 ten-second averages of ice spectra data and applied a rescaling technique to derive the following number density function for snow that was adopted in the new bulk microphysics scheme:

$$N(D) = \frac{\mathcal{M}_2^4}{\mathcal{M}_3^3} \left[ \kappa_0 e^{-\frac{\mathcal{M}_2}{\mathcal{M}_3} \Lambda_0 D} + \kappa_1 \left( \frac{\mathcal{M}_2}{\mathcal{M}_3} D \right)^{\mu_s} e^{-\frac{\mathcal{M}_2}{\mathcal{M}_3} \Lambda_1 D} \right], \quad (1)$$

where  $\kappa_0$ ,  $\kappa_1$ ,  $\Lambda_0$ ,  $\Lambda_1$ , and  $\mu_s$  are constants given in appendix B, and  $\mathcal{M}_n$  is the  $n$ th moment of the distribution given by

$$\mathcal{M}_n = \int D^n N(D) dD. \quad (2)$$

The first term in brackets in Eq. (1) represents an exponential form whereas the second term represents a gamma distribution. The sum of these two distributions accounts for the frequently observed “superexponential” number of small particles as well as the general slope of the large particles, as seen in Fig. 2. Note in Fig. 2 that an exponential distribution assumption will underestimate (overestimate) the number of small (large) ice particles. Through the use of Eq. (1), the effective  $y$ -intercept parameter depends on both the snow mix-

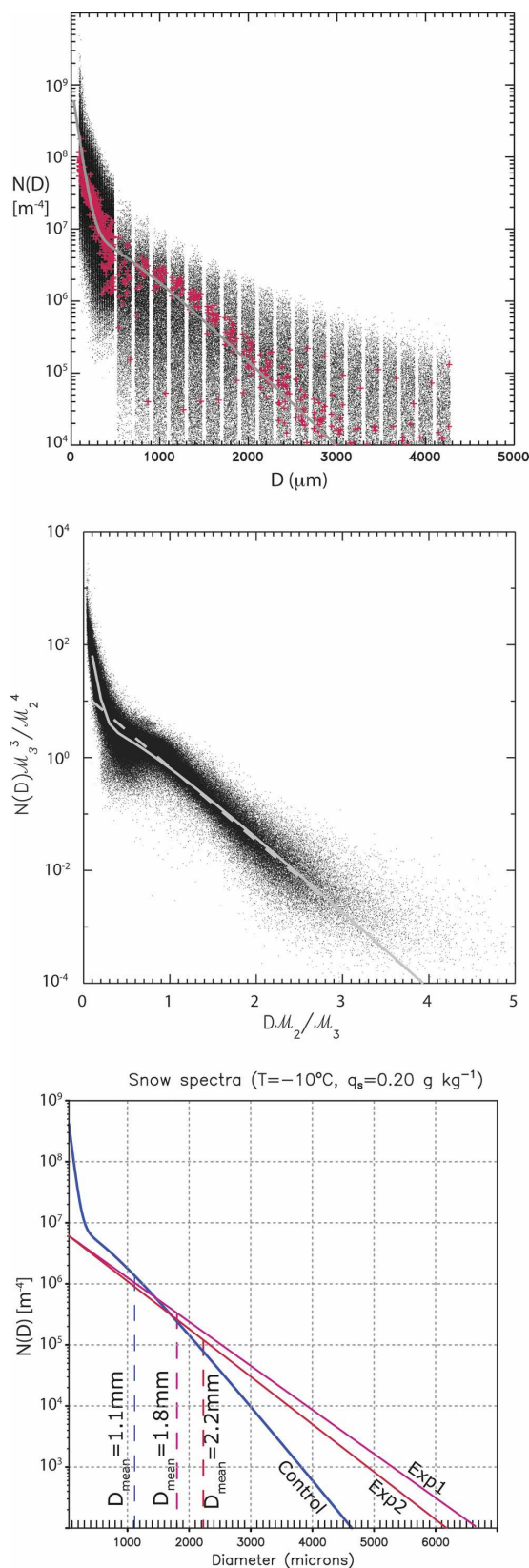
ing ratio and temperature, in a sense combining the concepts proposed in both Reisner et al. (1998) and Part I.

In addition, Field et al. (2005) provided simple power-law relations and constants to precompute various moments of the particle size distribution (PSD) when only the temperature and snow content are known. This simplifies some of the microphysical production–depletion rates like riming, depositional growth, and sedimentation. An example computation is provided in appendix C to illustrate the use of Field et al.'s moment relations in determining depositional growth. Using these moments also has the added advantage that bulk snow density is correctly modeled to have an inverse diameter dependence (Fig. 1) in contrast to most schemes that assume a constant snow density. Finally, the scheme is coded to allow model users to alter easily the mass-diameter or velocity-diameter relations, or the assumed shape of the distribution, without recoding any of the microphysical process rates.

Snow forms in the new scheme by vapor depositional growth onto cloud ice particles until those ice crystals grow beyond a threshold size (currently 200  $\mu\text{m}$ ). The threshold itself is relatively arbitrary and certainly artificial but allows for slowly falling tiny ice crystals to coexist with more rapidly falling snow. The current size threshold was chosen to be near the rime onset threshold (Pruppacher and Klett 1997), similar to other BMPs (Walko et al. 1995; Morrison and Pinto 2005), and near the size threshold of particles considered in Field et al. (2005) due to known detectability limits of two-dimensional cloud (2D-C) probes. With this scheme's relatively small cloud ice category, researchers verifying model-derived radiances versus those measured by satellite are strongly encouraged to include both the cloud ice and snow species since the snow size distribution overlaps the cloud ice category.

Another unique aspect of the new snow parameterization pertains to snow accreting cloud droplets or riming. Rather than utilize a constant collection efficiency of 100% like most other BMPs, the new scheme applies a variable efficiency based on the median volume diameter of snow and cloud water after Wang and Ji (2000). Efficiencies are precomputed based on broad-branched crystals at the start of the simulation and stored in a table.

Finally, the constants for computing the snow terminal velocity were chosen to match vertically pointing Doppler radar data (A. Heymsfield 2006, personal communication) and observations by Mitchell and Heymsfield (2005). Sensitivity tests using power-law constants from Brandes et al. (2007) and Locatelli and



Hobbs (1974) did not verify as well against the vertically pointing radar data.

### 3. Results of sensitivity experiments

#### a. Shallow/warm cloud system

As a first test of the new scheme, we repeated the 2D, idealized flow over a hill as previously reported in Part I. The WRF (version 2.2) Model was configured identically to match the MM5 setup including the four input thermodynamic profiles (see Fig. 5 in Part I) and idealized two-dimensional flow field and mountain barrier. Consistent with Part I, the WRF model domain was 120 points wide with 10-km spacing and 39 stretched vertical levels, and simulations were run without considering radiation, turbulence, or surface friction. Flow of  $15 \text{ m s}^{-1}$  impinging upon an idealized bell-shaped mountain 1 km high with a 100-km half-width. The temperature profiles for the four input conditions were kept constant, but the cloud height and temperature were readily modified by increasing the humidity to near saturation from the surface to various altitudes. As such, the simulations were designed to create progressively colder clouds with minimum temperatures of  $-13^\circ$ ,  $-25^\circ$ , and  $-60^\circ\text{C}$ . The fourth thermodynamic input used the lowest temperature but reduced the humidity below ice saturation for a 2-km-deep layer to mimic a “seeder-feeder” type event. Finally, the number concentration of cloud droplets was set to  $100 \text{ cm}^{-3}$ , which was consistent with simulations performed in Part I.

The Control experiment utilized the entire new bulk scheme as described in the previous section and the appendixes. Cloud water, rain, and snow mixing ratios at 3 h from the Control simulation are shown in Fig. 3 and reveal the same basic characteristics of the previous work except that direct numerical comparisons are not warranted because of the change from MM5 to WRF. Instead, this Control experiment was compared to various alternative representations of the snow size dis-

←

FIG. 2. (top) Plot of  $\sim 9000$  ten-second ice PSDs from Field et al. (2005) before applying a scaling technique. Special markers (plus signs) are used for observations within  $0.1^\circ\text{C}$  of  $-10^\circ\text{C}$  and within  $0.01 \text{ g kg}^{-1}$  of  $0.2 \text{ g kg}^{-1}$ . The thin gray line represents the model-assumed distribution for that temperature and snow content using Eq. (1). (middle) The distribution after scaling, along with the more typical exponential distribution assumption (dashed line). (bottom) The parameterized snow distributions from experiments Control, Exp1, and Exp2 and the associated mass-weighted mean size assuming  $T = -10^\circ\text{C}$  and  $q_s = 0.2 \text{ g kg}^{-1}$ .

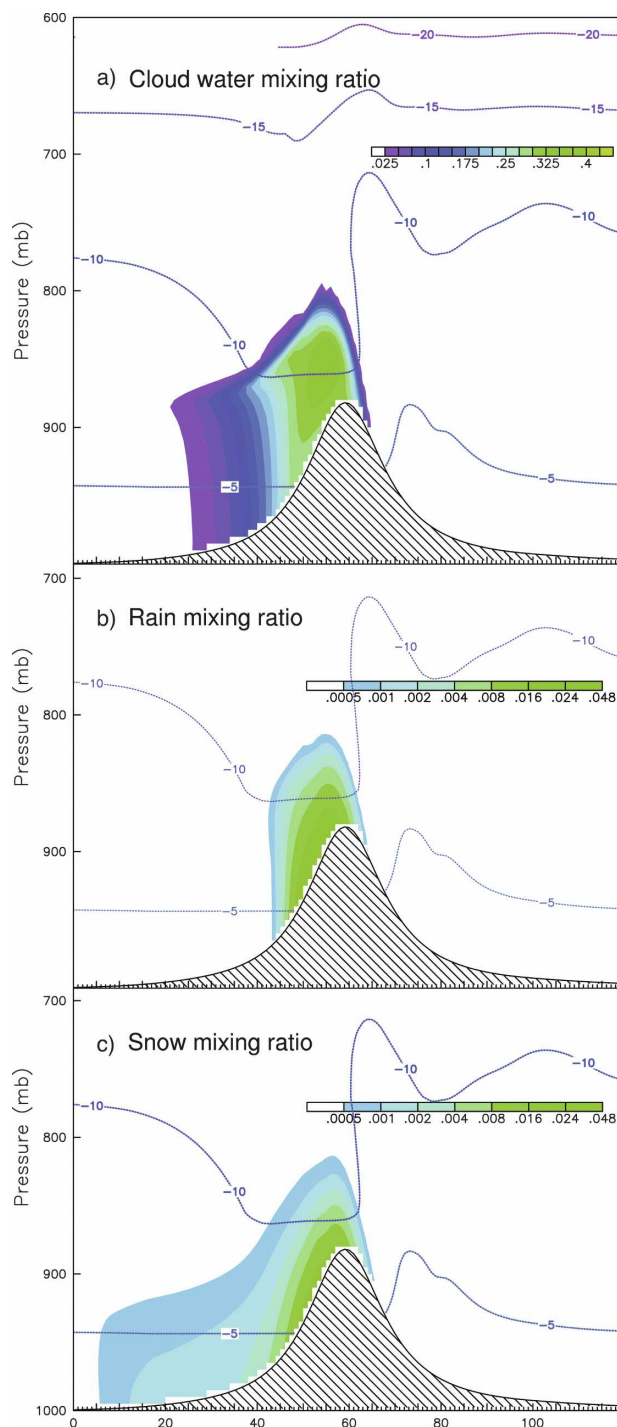


FIG. 3. Vertical cross sections from Control at 3 h using the CTT =  $-13^{\circ}\text{C}$  cloud system with temperature and (a) CLW, (b) rain, and (c) snow mixing ratios ( $\text{g kg}^{-1}$ ). Each grid point represents 10 km.

tributions and particle shapes in the subsequent sensitivity experiments including one experiment designed to compare the snow size distribution and assumed particle habit from Part I.

In experiment Exp1, the size distribution function [Eq. (1)] was reverted to an exponential form as nearly all other BMPs are configured, and the y-intercept parameter varied with temperature as found in Part I. Otherwise, the mass-diameter relation for snow and the implicitly variable snow density remained the same as in Control (i.e., nonspherical). In experiment Exp2, the assumed size distribution parameters remained the same as in Exp1, but the mass-diameter relation assumed the typical spherical habit with constant density ( $\rho_s = 100 \text{ kg m}^{-3}$ ). In experiment Exp3, all parameters remained the same as Exp2 except that the y-intercept parameter depended on the snow mixing ratio as found in Reisner et al. (1998). In this manner, the new scheme was progressively altered to older snow particle shape and size distribution assumptions. Refer to Table 1 for a summary of the parameters used in the four experiments.

The relatively shallow/warm cloud [cloud-top temperature (CTT) =  $-13^{\circ}\text{C}$ ] produced an obvious trend in terms of glaciation or ice-liquid ratio. Referring to Table 2, Exp3 produced the most snow and least supercooled liquid water (SLW), resulting in the most efficient precipitation. Though the 6-h accumulated precipitation was very small ( $\sim 1 \text{ mm}$ ), Exp3 produced 15% more precipitation than Exp2. Correspondingly, Exp3 had only 66% of Exp2's SLW. Next in the glaciation rankings were Control and Exp1, with slightly more SLW resulting in 7% less precipitation in the latter experiment. Contrasting the most glaciated (Exp3) to the least (Exp1), the differences appear significant with nearly twice as much SLW in Exp1 and roughly two-thirds of Exp3's precipitation.

Table 2 only reveals a single instant of time and only the domain-maximum hydrometeor mixing ratio, whereas a better illustration of the sensitivities is presented using contour frequency versus altitude diagrams (CFADs), as shown in Fig. 4. The abscissa consists of quantities of the hydrometeor mixing ratio of cloud water, rain, and snow while the ordinate is the vertical model level (rather than the typical altitude since using the latter would compact the contours to a much smaller vertical extent due to the stretching used in the model's vertical coordinate). The frequency with which a grid point's mixing ratio exceeds the amount shown on the abscissa is contoured. The 25th–65th grid points were used (see Fig. 3) to create the CFADs because some cloud exists nearly continuously in this portion of the domain. The first 2 h were ignored to avoid any model spinup effects, leaving seventeen 15-min intervals included in the CFADs.

Figure 4 confirms that Exp3 was the most glaciated, followed by Exp2, then Control, and finally Exp1. The

TABLE 1. Experiment name, mass–diameter power law, and assumed distribution shape.

Expt name	Sphericity/density assumption	Number distribution function
Control	Nonspherical, variable density ( $0.069D^2$ )	Sum of exponential + gamma [Eq. (1)]
Exp1	Nonspherical, variable density ( $0.069D^2$ )	Exponential [with $N_0$ following Part I; Eq. (13)]
Exp2	Spherical, constant density ( $\pi\rho_s D^3/6$ )	Exponential [with $N_0$ following Part I; Eq. (13)]
Exp3	Spherical, constant density ( $\pi\rho_s D^3/6$ )	Exponential [with $N_0$ following Reisner et al. (1998); Eq. (5)]

minimal presence of cloud water in Exp2 and Exp3 clearly accounted for the nearly nonexistent rain, essentially freezing drizzle. Both Control and Exp1 produced freezing drizzle and were very similar overall with slightly higher amounts of snow found in Control. The latter experiment produced more snow than Exp1 due to the more numerous small particles when using the distribution function in Eq. (1) (refer to Fig. 2). Consequently, the mass-weighted terminal velocity of snow in Control was less than that found in Exp1 and contributed to higher snow amounts in Control.

The sensitivity experiments that assumed nonspherical snow, namely Control and Exp1, produced more SLW and less snow than the experiments that assumed spherical snow. Was this due to riming growth, depositional growth, or sedimentation? The two growth processes are controlled by the particle number and surface area and a sphericity assumption for snow minimizes the particle surface area; therefore, Exp2 and Exp3 should have the least snow and the most water, yet our results revealed the exact opposite. Sedimentation is directly related to mass-weighted mean size but subsequently impacts riming due to geometric sweep-out and depositional growth due to ventilation.

A closer analysis of the first 30 min of simulations Exp1 and Exp2 showed the domain-maximum snow mixing ratio grew from  $0.31 \times 10^{-10} \text{ g kg}^{-1}$  at 600 s to  $0.42 \times 10^{-8} \text{ g kg}^{-1}$  at 1200 s to  $0.35 \times 10^{-7} \text{ g kg}^{-1}$  at 1800 s in Exp1. All of this growth occurred due to vapor deposition while the riming remained negligible due to

the very small size of the snow. Meanwhile, in Exp2, the snow mixing ratio progressed from  $0.19 \times 10^{-9} \text{ g kg}^{-1}$  to  $0.19 \times 10^{-6} \text{ g kg}^{-1}$  to  $0.95 \times 10^{-6} \text{ g kg}^{-1}$  at the same respective times. In under 30 min, the snow amount in Exp2 was nearly 50 times that in Exp1 and the discrepancy further accelerated as riming growth commenced.

Recall that Exp1 and Exp2 both assumed an exponential distribution with the temperature-diagnosed y-intercept parameter. Exp2 assumed constant-density spheres whereas Exp1 assumed variable density, nonspherical particles. The assumed bulk density resolves the preceding contradiction. As mentioned in section 2, Exp1 (and also Control) retained the inverse relationship between particle density and diameter ( $\rho_s = 0.13D^{-1}$ ) whereas Exp2 and Exp3 assumed a constant value (see also Fig. 1). In the first 30 min of Exp1, the low mixing ratios of snow correlated to very small particle diameters with relatively high densities, from 2 to 8 times higher density than the constant value used by Exp2 and Exp3. Therefore, for a given snow mixing ratio, the mass-weighted mean size of Exp2's constant-density spherical snow was larger than the higher-density, nonspherical snow of Exp1, resulting in faster depositional growth and faster sedimentation in Exp2. A similar deduction can be made regarding riming. Refer to Fig. 7, described below, for a plot showing the mass-weighted mean size of snow from Control and Exp1, and its associated density variation with size.

The integrated effects of these sensitivities are readily illustrated using a vertical column near the

TABLE 2. Domain-maximum hydrometeor quantities and accumulated precipitation at 6 h from 2D sensitivity experiments.

Expt name	Cloud system	$q_c$ ( $\text{g kg}^{-1}$ )	$q_r$ ( $\text{g kg}^{-1}$ )	$q_s$ ( $\text{g kg}^{-1}$ )	Precipitation (mm)
Control	CTT = $-13^\circ\text{C}$	0.329	0.018	0.035	0.73
	CTT = $-25^\circ\text{C}$	0.117		0.127	2.93
	CTT = $-60^\circ\text{C}$	0.088		0.150	3.58
Exp1	CTT = $-13^\circ\text{C}$	0.330	0.021	0.019	0.68
	CTT = $-25^\circ\text{C}$	0.174		0.101	2.66
	CTT = $-60^\circ\text{C}$	0.148		0.115	3.37
Exp2	CTT = $-13^\circ\text{C}$	0.267	0.002	0.027	0.85
	CTT = $-25^\circ\text{C}$	0.202		0.084	2.78
	CTT = $-60^\circ\text{C}$	0.182		0.101	3.39
Exp3	CTT = $-13^\circ\text{C}$	0.177	0.001	0.036	0.98
	CTT = $-25^\circ\text{C}$	0.140		0.089	2.74
	CTT = $-60^\circ\text{C}$	0.126		0.106	3.26

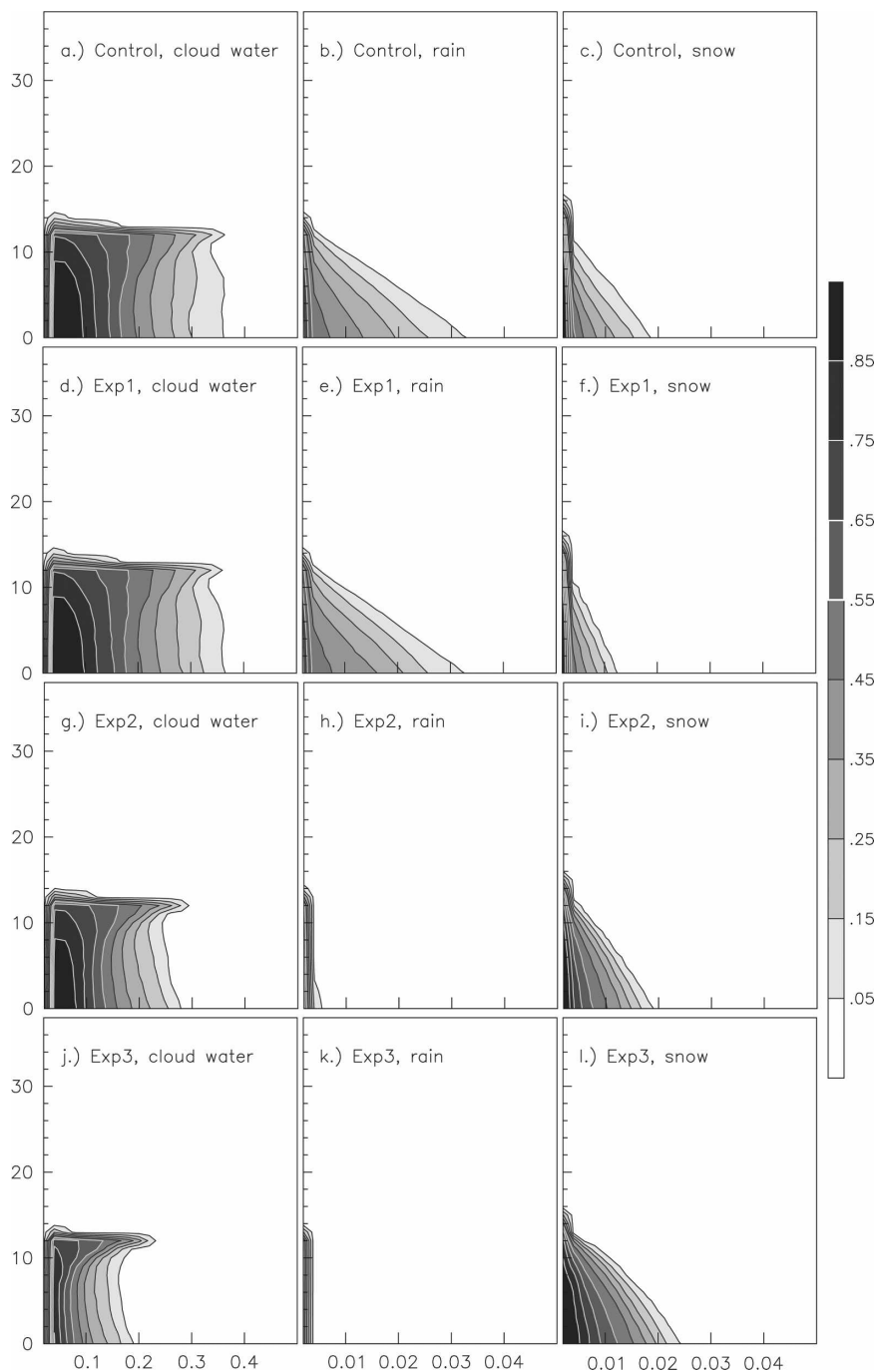


FIG. 4. CFAD from the shallow/warm cloud system ( $CTT = -13^{\circ}\text{C}$ ) from the (a)–(c) Control, (d)–(f) Exp1, (g)–(i) Exp2, and (j)–(l) Exp 3 sensitivity experiments. Each row shows cloud water, rain, and snow mixing ratio on the abscissa and vertical model level on the ordinate. Contours and shading represent frequency with which the hydrometeor mixing ratio exceeded the amount shown on the abscissa between forecast hours 2 and 6 and between grid points 25 and 65.



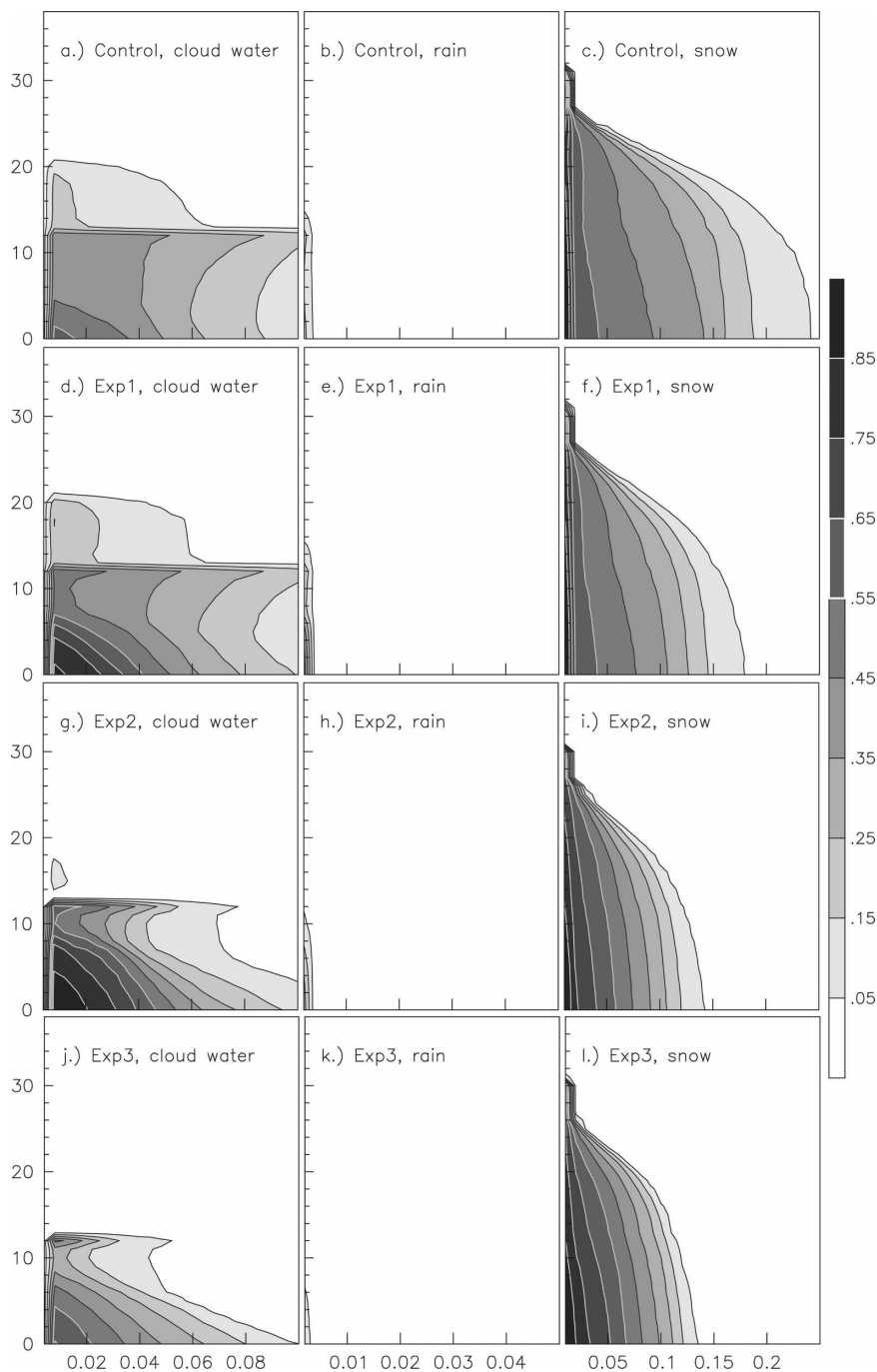


FIG. 5. As in Fig. 4 but from the deep/cold cloud system (CTT =  $-60^{\circ}\text{C}$ ) and the abscissas for cloud water and snow are altered.

maximum precipitation at 120 min that revealed the median volume diameter (MVD) of snow increasing from 337 to 735  $\mu\text{m}$  from near cloud top down to the surface in Exp1. At the same column and time as in Exp2, the MVD of snow increased from 1013 to 1633  $\mu\text{m}$ .

#### b. Deep/cold cloud system

Rerunning the tests with progressively deeper and colder cloud conditions did not reproduce the same trend seen in the shallow/warm cloud. The tests with cloud-top temperatures of  $-25^{\circ}$  and  $-60^{\circ}\text{C}$  revealed



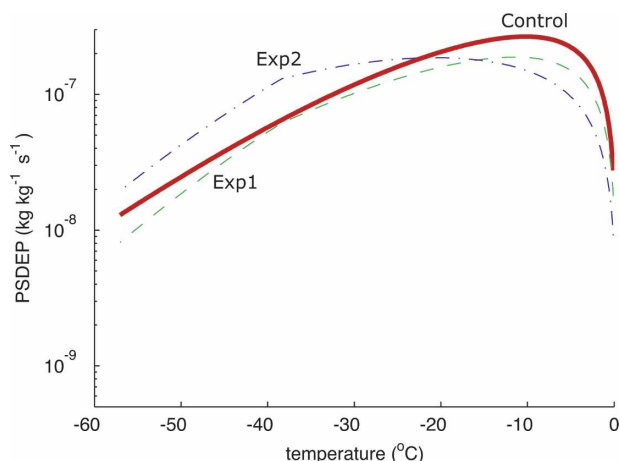


FIG. 6. Depositional growth of snow vs temperature assuming the snow mixing ratio decreases from  $0.5 \text{ g kg}^{-1}$  at  $T = 0^\circ\text{C}$  to  $0.05 \text{ g kg}^{-1}$  at  $T = -60^\circ\text{C}$  and nearly water saturated (i.e., the same conditions as were used in Part I, Fig. 3b) but for the sensitivity experiments: Control, Exp1, and Exp2.

similar characteristics to each other that differed from the shallow/warm cloud, but they can be jointly illustrated with the results of the coldest cloud.

These cold cloud simulations had nearly identical precipitation amounts, and their maximum snow amounts were very similar with broader snow coverage aloft in Exp2 and Exp3 relative to Exp1 or Control (not shown). In contrast to the shallow cloud, Exp2 had the highest SLW followed by Exp1, then Exp3, and finally Control. Even though the Control experiment had 42% more snow aloft than the experiment with the least snow (Exp2), the resulting precipitation at the ground was only 6% different between the two. The same 42% difference in snow reduced the SLW by 30% in Control versus Exp2.

The tendency for the Control experiment to glaciate more readily than the others is best illustrated by the CFADs for the CTT =  $-60^\circ\text{C}$  cloud system in Fig. 5. Similar to the shallow/warm cloud system, Exp1 resembled Control whereas Exp2 and Exp3 were more similar to each other than they were to the other two. The larger amount of snow in Control above the inversion was due to the more numerous small particles diagnosed by Eq. (1). These more numerous small particles were responsible for both reduced sedimentation and increased vapor depositional growth in Control relative to Exp1 as shown by Fig. 6, which shows the depositional growth rate in Control exceeds that of Exp1.

Unlike the shallow/warm cloud system, the variable snow density found in Control was responsible for an increase in the deposition and riming rates relative to

Exp2. Chronologically, snow initiated in Control with numerous small particles due to the assumed distribution shape and grew larger by vapor deposition. Compare Fig. 7c with Fig. 7d, which shows that the mass-weighted mean size of the snow is larger in Control from cloud top down to roughly 500 hPa versus Exp1. These larger snowflakes were then responsible for more efficient riming in the liquid cloud below the inversion and more rapidly depleted the SLW, which is why Control had much less SLW than Exp1. In contrast to the shallow cloud, the relatively high constant-density, spherical snow of Exp2 was less efficient in removing SLW, which is why Exp2 had larger amounts of cloud water and less snow than Exp1.

## 4. Discussion

When deciding which representation of snow to use in a microphysical parameterization, there are several points to consider: snow geometry, diagnostic method, and PSD shape.

### a. Snow geometry

Previously, spherical snow with a constant density of  $100 \text{ kg m}^{-3}$  has been used in many models (i.e., Lin et al. 1983; Reisner et al. 1998; Gilmore et al. 2004). While this is a good approximation for snow around 1.5 mm in diameter, it is far from realistic at either larger or smaller sizes (see Fig. 1). Recent theoretical work (Westbrook et al. 2004) and empirical observations (e.g., Locatelli and Hobbs 1974; Heymsfield and Kajikawa 1987; Mitchell et al. 1990; Heymsfield et al. 2007) suggest that the mass of snow is proportional to  $D^2$ , or alternatively, its bulk density is proportional to the inverse of its size. Therefore, it is more realistic to adopt a mass–dimension relation of the form  $m \propto D^2$ .

### b. PSD diagnostic method

Within a bulk microphysical scheme there are a limited number of predicted variables available that can be used to diagnose snow PSD properties. The most popular method is to use temperature to diagnose the  $y$  intercept of an exponential distribution based on the work of Houze et al. (1979). Another approach has been to relate the intercept parameter to snow content (e.g., Sekhon and Srivastava 1970). For this work, we defined the PSD by employing both temperature and snow content using orders of magnitude more observed PSDs than are found in either of the other references. We believe, that in this way, we are better able to reproduce more of the variability associated with the observed snow PSDs.

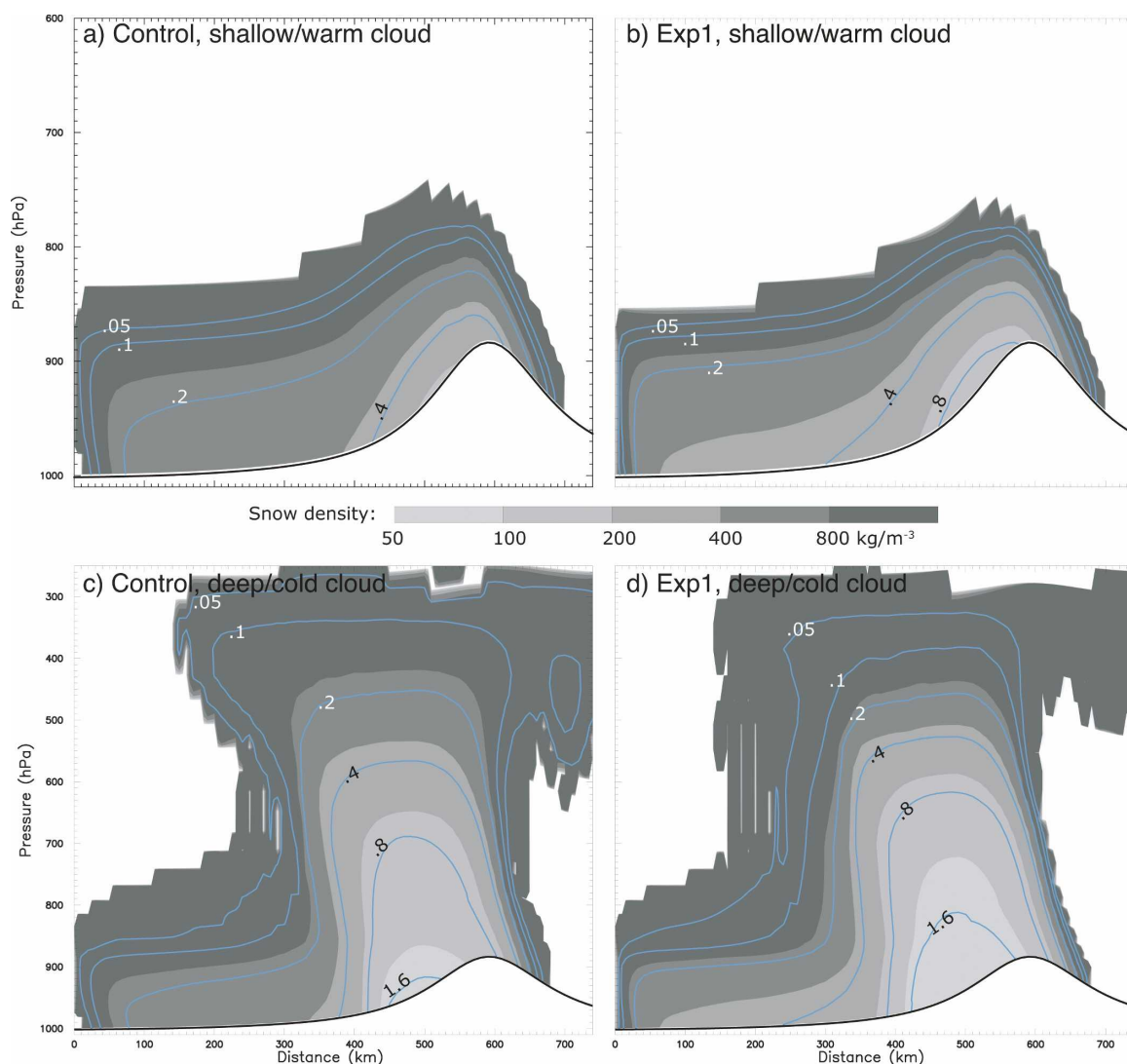


FIG. 7. Mass-weighted mean size (contours of diameter; mm) and density (gray shades) found in the Control and Exp 1 after 3 h for the shallow/warm and deep/cold cloud systems.

### c. PSD shape

In practice, the dominant shape assumption for the snow size distribution is exponential even when the shape is mathematically represented as a gamma distribution. Here, the Control PSD shape has been determined from a large database of measured PSDs using a rescaling technique to reveal the underlying shape. In this research, the Control PSD shape has an exponential tail and relatively high concentrations of small ( $D < 400 \mu\text{m}$ ) particles when compared to a pure exponential distribution (Fig. 2c). Two studies appear to confirm the utility of the Control PSD shape. Doherty et al. (2007) simulated satellite brightness temperatures ( $\sim 183 \text{ GHz}$ ) using model-predicted ice water content, with assumed PSD shape and mass-diameter relations,

as input into a radiative transfer model. They found that of the parameterizations examined, the combination of the Field et al. (2005) PSD and  $m = 0.069D^2$  mass-diameter relationship resulted in the best agreement versus observations for a range of measures. In the second study by Kim et al. (2007), radar measurements were combined with the Field et al. (2005) PSD representation to compute microwave brightness temperatures. They also found good agreement with satellite observations. Therefore, we believe this PSD representation could be used to form the basis of a consistent microphysics and assimilation suite.

The sensitivities found in the deep/cold idealized 2D cloud system were confirmed in a WRF simulation of a case study from the Microphysical Parameterization through Observational Verification Experiment

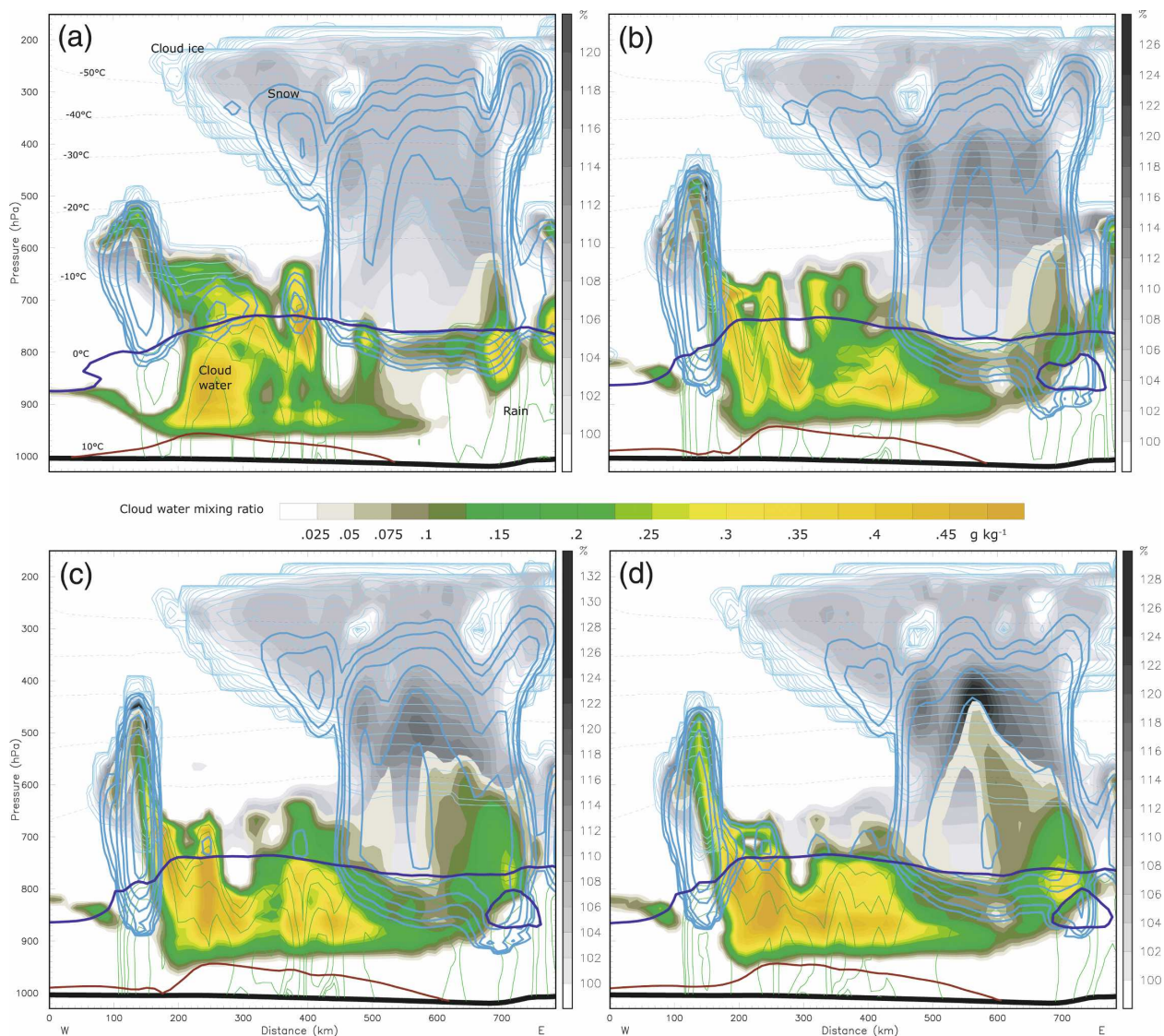


FIG. 8. WRF 22-h forecast valid 2200 UTC 1 Feb 2001 showing a cross section along the A–A' line in Locatelli et al. (2005, Fig. 4a) from sensitivity experiments (a) Control, (b) Exp1, (c) Exp2, and (d) Exp3. Gray-shaded regions represent relative humidity with respect to ice (%) with varying scales shown at the right of each panel. Green and yellow shades represent cloud water mixing ratio ( $\text{g kg}^{-1}$ ). Other contours are labeled in (a) including temperature ( $^{\circ}\text{C}$ ), cloud ice (cyan), snow (blue), and rain (green). Note, in general, that the lowest humidity is found in Control.

(IMPROVE-1) field project (Stoelinga et al. 2003). Details of the simulation and a more complete comparison to observations are found in the forthcoming Part III of this paper, but the sensitivity of the four experiments in relation to the 2D results are briefly discussed here. The tendency for the Control experiment to glaciate deep/cold synoptic-scale frontal clouds more so than the other experiments is revealed in a plot of hydrometeors and relative humidity with respect to ice found in Fig. 8. Control produced the least saturation with respect to ice whereas Exp3 produced the highest saturation, even reaching water saturation and producing cloud water.

The Control experiment produced minimal liquid cloud between  $0^{\circ}$  and  $-10^{\circ}\text{C}$ , in a relatively narrow updraft region; otherwise, the storm was dominated by moderate snow content ( $0.2\text{--}0.4 \text{ g kg}^{-1}$ ). Exp1 produced only slightly more cloud water to higher altitudes around 800–600 hPa and, correspondingly, less snow content overall. Consistent with the 2D results, Exp1 had slightly higher ice supersaturations but was otherwise similar to Control. Exp2 had higher (lower) amounts of cloud water (snow) and much higher ice supersaturation beginning to depart from the observations (of this case) found in Locatelli et al. (2005) and Evans et al.

TABLE A1. Mass and terminal velocity constants for each liquid/ice species.

Hydrometeor	Coefs in Eq. (2)		Reference	Coefs in Eq. (3)			Reference
	$a$	$b$		$\alpha$	$\beta$	$f$	
Cloud water	$\pi\rho_w/6$	3	—	—	—	—	—
Rain	$\pi\rho_w/6$	3	—	4854	1	195	Ferrier (1994)
Cloud ice	$\pi\rho_i/6$	3	—	1847.5	1	0	See text
Snow	0.069	2	Cox (1988)	40	0.55	125	See text
Graupel	$\pi\rho_g/6$	3	Reisner et al. (1998)	442	0.89	0	Heymsfield and Kajikawa (1987)

(2005). The results of Exp3 are not consistent with observations at all, with liquid cloud reaching above the altitude of  $T = -20^\circ\text{C}$  and very high ice supersaturations. Again, more detailed analyses of this model simulation and simulations of other cases will be presented in Part III.

## 5. Future work

The most immediate plans for the scheme include the prediction of cloud water and rain number concentrations. Cloud water will activate on an assumed aerosol distribution that, at minimum, will differentiate the continental versus maritime horizontal model points as well as vary the aerosol amounts in the vertical based on points being within or above the planetary boundary layer. Beyond this, we hope to initialize the aerosol number concentration from Moderate Resolution Imaging Spectroradiometer (MODIS) or other satellite-derived data. The assumed aerosol composition will start out simplistically but has the potential for added complexity by closely linking the microphysics scheme to the WRF chemistry model. Another potential improvement is an explicit treatment for melting snow and graupel to produce the correct terminal velocities of these species below the melting level.

**Acknowledgments.** The authors thank G. Bryan, I. Geresdi, U. Blahak, H. Morrison, A. Heymsfield, B. Bernstein, E. Brandes, K. Ikeda, C. Woods, R. Wood, B. Lynn, S. Ghan, and M. Gilmore for their input. This research is in response to requirements and funding by the Federal Aviation Administration. The views expressed are those of the authors and do not necessarily represent the official policy or position of the FAA.

## APPENDIX A

### Bulk Microphysical Parameterization Description

#### a. Water and ice species

The new bulk microphysics scheme departs from other WRF/MM5 BMPs by assuming each hydromete-

or species (except snow) conforms to a generalized gamma distribution (Walko et al. 1995; Verlinde et al. 1990):

$$N(D) = \frac{N_t}{\Gamma(\mu + 1)} \lambda^{\mu+1} D^\mu e^{-\lambda D}, \quad (\text{A1})$$

in place of the exponential distribution. In Eq. (A1),  $N_t$  is the total number of particles in the distribution,  $D$  is the particle diameter,  $\lambda$  is the distribution's slope, and  $\mu$  is the shape parameter. When  $\mu = 0$ , the distribution becomes the classic exponential (or Marshall–Palmer) distribution.

All water and ice species use the relatively standard power-law form to describe their mass and terminal velocity as a function of diameter. Specifically, the mass relation is given by

$$m(D) = aD^b, \quad (\text{A2})$$

whereas the velocity relation follows Ferrier (1994),

$$v(D) = \left(\frac{\rho_0}{\rho}\right)^{1/2} \alpha D^\beta e^{-fD}, \quad (\text{A3})$$

along with his use of the exponential to handle the large particles better than the straight power law. The constants used in Eqs. (A2) and (A3) for all hydrometeors are summarized in Table A1. Only cloud water does not sediment, and the two liquid species use the obvious spherical assumption where  $\rho_w = 1000 \text{ kg m}^{-3}$  is the density of water.

The individual species are described in more detail in the subsections below. In the remainder of the text, the subscripts  $c$ ,  $i$ ,  $r$ ,  $s$ , and  $g$  represent cloud water, cloud ice, rain, snow, and graupel species, respectively. For example,  $\mu_c$  represents the shape parameter for the cloud water distribution. Furthermore, unless specifically noted otherwise, all equations and constants given in the text assume Système International (SI) units.

#### 1) CLOUD WATER

As found in nearly all of the alternative BMPs in WRF/MM5, the new scheme requires presetting the number of cloud droplets that get activated upon con-



densation. In the future, the droplet concentration will be predicted by explicit activation of aerosols, but it is currently set to a constant at the start of the model run. For simplicity, the current code uses  $N_c = 100 \text{ cm}^{-3}$ , which represents rather “clean” air often found above the planetary boundary layer and/or near oceanic regions. Users are strongly advised to set  $N_c$  according to known data because of the direct dependencies between droplet number, mean size, and resulting conversion to rain.

Previous BMPs, like those in Reisner et al. (1998), Part I, and Hong et al. (2004), assumed a monodisperse population of cloud droplets. With the new gamma distribution for cloud water, a value for the shape parameter  $\mu_c$  must be set or calculated. In field studies, Martin et al. (1994) found the relative dispersion of droplets to be 0.25 in clean maritime air masses and 0.45 in more polluted continental air masses. Since we generally assume that maritime air masses have low droplet concentrations of roughly  $75\text{--}100 \text{ cm}^{-3}$  while continental air masses have concentrations of  $250 \text{ cm}^{-3}$  or more, we derived the following empirical relationship between number concentration  $N_c$  and  $\mu_c$  to match those observations of relative dispersion:

$$\mu_c = \min\left(15, \frac{10^9}{N_c} + 2\right). \quad (\text{A4})$$

## 2) CLOUD ICE

As with cloud water, cloud ice also assumes the generalized gamma form of Eq. (A1), but since its number concentration is predicted, its shape parameter is the only free parameter that needs to be preset. At this time, we have little observational guidance for setting the value of  $\mu_i$  so we recommend setting it between 0 and 2 inclusive. In the future, we hope field project campaigns will provide more insight into the small ice size distribution characteristics.

As a double-moment species, cloud ice does have differential sedimentation whereby the mixing ratio and number concentration use their respective mass-weighted and number-weighted terminal velocities. Its terminal velocity constants were chosen to produce a smooth transition from the cloud ice to snow category at the snow threshold diameter.

Since double-moment species are prone to imbalances between mass and number concentration, cloud ice number is constrained such that its mass-weighted mean size is bound between approximately 30 and 300  $\mu\text{m}$ . This upper limit is rarely, if ever, exceeded because of the technique to transfer the largest cloud ice particles into the snow category (details found in section b4 of this appendix).

## 3) RAIN

Unique to this microphysics scheme, the rain size distribution significantly shifts depending on whether the rain *appears* to originate from melted ice versus rain produced by the collision-coalescence (warm rain) process. After rearranging terms in Eq. (A1), the gamma size distribution is expressed in a simple form as

$$N(D) = N_0 D^\mu e^{-\lambda D}, \quad (\text{A5})$$

where  $N_0$  is the “intercept parameter” of the distribution. When  $\mu = 0$ ,  $N_0$  is the physical y intercept of an exponential distribution; however, when  $\mu > 0$ , this parameter has no physical interpretation. Whereas most BMPs assume rain follows an exponential distribution with a constant  $N_0 = 8 \times 10^6 \text{ m}^{-4}$ , we slightly modified Thompson et al.’s [(2004); Eq. (14)] variable intercept parameter to use

$$N_{0,r} = \left(\frac{N_1 - N_2}{2}\right) \tanh\left[\frac{(q_{r0} - q_r)}{4q_{r0}}\right] + \frac{N_1 + N_2}{2}, \quad (\text{A6})$$

where  $N_1 = 9 \times 10^9 \text{ m}^{-4}$  is an upper intercept limit,  $N_2 = 2 \times 10^6 \text{ m}^{-4}$  is a lower intercept limit, and  $q_{r0} = 1 \times 10^{-4} \text{ kg kg}^{-1}$  is essentially the transition value between the two limits. To apply this equation, we begin with the model’s predicted rain mixing ratio and use Eq. (A6) to diagnose the exponential size distribution’s intercept parameter. Then, we convert to the correct  $N_0$  parameter for the gamma distribution by assuming the two distributions have the same mass and number concentration.

Using a variable intercept parameter was done to mimic conditions of drizzle as well as larger raindrops. Unlike in Part I, however,  $N_{0,r}$  also depends on the presence of melted snow and graupel in a column above the uppermost melting level. If, after consulting a vertical column, there is snow and/or graupel at the first level above and rain at the first level below the level where melting begins, then the column is searched for the bottom of the melting layer whereby the snow and graupel are effectively completely melted.

Below this melting layer, the mass-weighted mean size of rain is set to the same mass-weighted mean size of melted snow or graupel (whichever is larger but restricted to no larger than 2.5-mm MVD). At the top of the melting layer, the MVD of rain is set to the maximum computed using  $N_{0,r}$  in Eq. (A6) (and converted to the gamma form) and 50  $\mu\text{m}$ . Then, the MVD is linearly increased until reaching the bottom of the entire melting layer.

In this way, for a pure classical precipitation scenario

of ice falling through a melting layer, the MVD for rain increases from  $50\ \mu\text{m}$  at the start of the melting layer to the melted ice equivalent diameter by the bottom of the melting layer. Essentially, we are able to mimic the melting of snow in which the smallest flakes melt into small drops first followed by the larger flakes. Using the classic Marshall–Palmer constant  $N_{0,r}$  tends to make the rain fall much too quickly as snow begins melting.

Alternatively, in a nonclassical, warm rain precipitation-formation scenario, very low drizzle production will result from cloud droplet collision–coalescence and the intercept parameter will be very large [by Eq. (A6)] thereby indicating the dominance of small drops in the distribution (and attendant low terminal velocity). But, as those drizzle drops fall and accrete more cloud water, the rain mixing ratio will increase and the  $N_0$  parameter will decrease, thus shifting the distribution toward larger sizes.

Finally, in the mixed-phase case with both warm rain production (above the melting level) and snow, we choose the larger of the computed MVD and  $50\ \mu\text{m}$  and apply it to the melting level. From that level to the bottom of the melting layer, the MVD is linearly increased to the melted ice equivalent size. In this manner, the MVD for rain would not abruptly change across the melting level.

#### 4) SNOW

See section 2 in the main body of the paper.

#### 5) GRAUPEL

Similar to rain, the new BMP's graupel species also contain a variable intercept parameter in order to capture graupel-like snow and higher-density (and faster falling) hail. Nearly all BMPs based on Lin et al. (1983) use a constant  $N_0$  set relatively high (classical value is on the order of  $10^6\ \text{m}^{-4}$ ) nearly matching that of snow. Interestingly, the Goddard BMP (Braun and Tao 2000) has an internal piece of code to shift the density and  $N_0$  parameters of graupel to act more like a hail distribution with two to three orders of magnitude lower  $N_0$ . Gilmore et al. (2004) showed how sensitive the QPF (and storm evolution) can be to this single aspect.

In this new scheme, we diagnose the intercept parameter from the graupel mixing ratio. Conceptually, we believe strong updrafts capable of producing large amounts of cloud water, rain, and snow result in more graupel than that produced by weak updrafts. By significantly reducing the  $N_0$  parameter, the graupel spectrum shifts to larger sizes and its mass-weighted mean fall speed increases more rapidly than can be done with a constant  $N_0$  and an increased mixing ratio. Similar to

Part I, the new BMP uses a relationship between the mixing ratio,  $q_g$ , and  $N_{0,g}$  given by

$$N_{0,g} = \max\left[10^4, \min\left(\frac{200}{q_g}, 5 \times 10^6\right)\right]. \quad (\text{A7})$$

While it would be ideal to alter the density of the graupel from a relatively low value characteristic of rimed snow to a higher value characteristic of hail, we set its density constant ( $400\ \text{kg m}^{-3}$ ) at this time. Factor of 2 changes to the density had a minimal effect on 12-h storm simulations compared to the massive effects when changing  $N_{0,g}$ .

The terminal velocity constants for graupel are taken directly from Heymsfield and Kajikawa (1987). These constants cause low mixing ratios of graupel to fall roughly twice as fast as snow but, with the higher mixing ratios and computed lower intercept parameters, graupel falls more rapidly and approaches speeds more characteristic of hail. Fig. A1 shows a plot of the terminal velocity of all hydrometeors. Note the nonlinear fall speed of graupel and rain due to the variable intercept parameters. The rain and snow terminal velocities level off because of the nonzero exponential constant  $f$  in Eq. (A3).

### b. Microphysical processes

In this section we describe the microphysical processes that are considered in the new bulk scheme. In subsections below the warm rain processes are detailed first, followed by ice initiation and growth mechanisms, then hydrometeor collection and sedimentation.

#### 1) CONDENSATION–EVAPORATION

Cloud water condenses only when water vapor exceeds the saturation threshold, which is determined using the polynomial approximation found in Flatau et al. (1992). As stated in the previous section, the number of droplets activated is preset by the user and remains constant in space and time. Research is under way to incorporate a more explicit nucleation scheme in a future version of the code. Whereas all other WRF/MM5 BMPs use an oversimplified saturation adjustment procedure (cf. Reisner et al. 1998), the new scheme uses a more accurate Newton–Raphson iterative technique (Langlois 1973) to solve the Clausius–Clapeyron equation.

Cloud water evaporation is handled by the saturation adjustment scheme mentioned above whereas rain evaporates following Srivastava and Coen [(1992); Eq. (16)]. Their method is more accurate specifically for rain falling into hot and dry air masses compared to earlier treatments. Vapor depositional growth of rain is

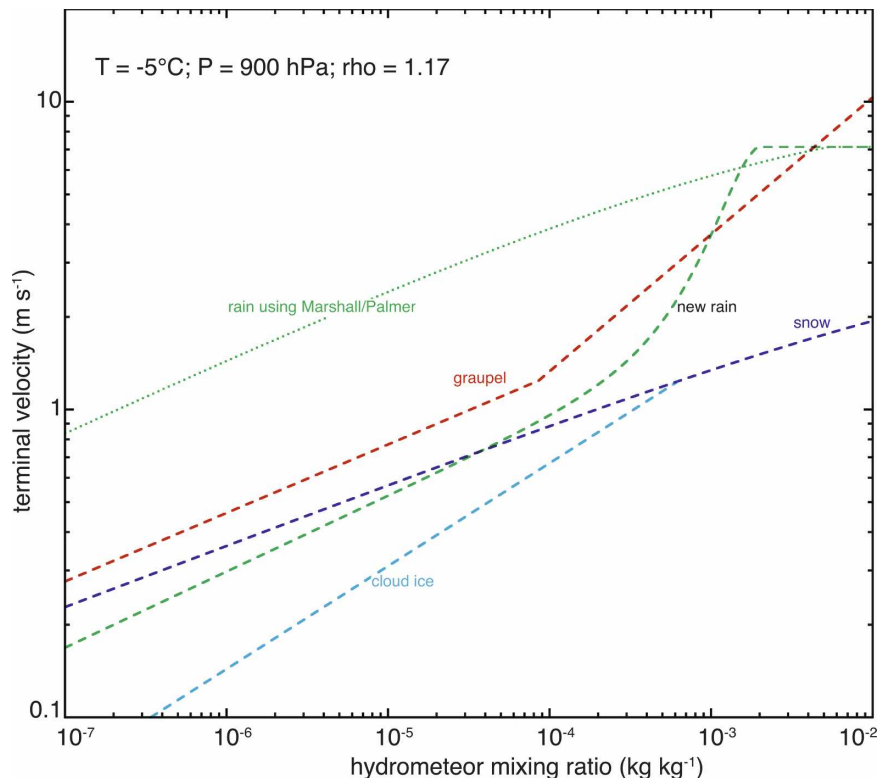


FIG. A1. Mass-weighted particle terminal velocity vs mixing ratio for hydrometeor species: cloud ice, snow, graupel, and rain at 900 hPa and  $T = -5^{\circ}\text{C}$ . The dotted line labeled “rain using Marshall–Palmer” indicates the terminal velocity for rain using a constant value of  $N_0 = 8 \times 10^6 \text{ m}^{-4}$ , while the dashed line labeled rain uses the mass-dependent relationship in Eq. (A6).

ignored since the saturation adjustment scheme will remove any supersaturation with respect to water by increasing the cloud water content instead of rain. Because of coding practices, some BMPs (e.g., Reisner et al. 1998; Hong et al. 2004) allowed rain to evaporate at the same time as cloud water even if evaporation of both leads back to water supersaturation. While coding this new scheme, we ensured that cloud water evaporates first and then rain evaporates only if subsaturated conditions remain.

## 2) AUTOCONVERSION

Without a higher-order microphysics scheme consisting of a number of explicit size bins of water drops, bulk schemes rely on parameterizations to determine when cloud water droplets grow sufficiently large to acquire appreciable fall speeds and become “rain.” This aspect is termed autoconversion and there is no shortage of treatments found in the literature. Many authors of bulk schemes start with one of the more classical treatments (Berry and Reinhardt 1974; hereinafter BR74) and make simplifying assumptions that sometimes end

up producing results hardly reflecting the original (Gilmore and Straka 2008). More recently, researchers employed fully explicit bin microphysical models to simulate the droplet collision–coalescence process and then derived empirical relationships to match those results for use in simpler bulk schemes (cf. Khairoutdinov and Kogan 2000).

In this new scheme, we attempted to keep the complete spirit of BR74 in which the characteristic diameters must be properly computed from the full assumptions of the distribution. Our only diversion from BR74 is that our assumed droplet spectrum follows the gamma distribution of Eq. (A1) whereas theirs followed a slightly different generalized Golovin distribution. Nonetheless, the important thing is to compute the proper characteristic diameters of the distribution. The amount of cloud water converting to rain per unit time is given by

$$\frac{dr_r}{dt} = \frac{0.027 \rho q_c \left( \frac{1}{16} \times 10^{20} D_b^3 D_f - 0.4 \right)}{\frac{3.72}{\rho q_c} \left( \frac{1}{2} \times 10^6 D_b - 7.5 \right)^{-1}}, \quad (\text{A8})$$



where the characteristic diameters,  $D_b$  and  $D_f$ , are derived from BR74 [Eqs. (1)–(6)]:

$$D_f = \left( \frac{6\rho q_c}{\pi\rho_w N_c} \right)^{1/3}, \quad (\text{A9})$$

$$D_g = \frac{\left[ \frac{\Gamma(\mu_c + 7)}{\Gamma(\mu_c + 4)} \right]^{1/3}}{\lambda_c}, \quad \text{and} \quad (\text{A10})$$

$$D_b = (D_f^3 D_g^3 - D_f^6)^{1/6}. \quad (\text{A11})$$

Sensitivity tests with this autoconversion treatment and a commonly used alternative (Khairoutdinov and Kogan 2000) showed very similar results in idealized 2D experiments as well as a handful of 3D case studies.

### 3) ICE NUCLEATION

Primary ice nucleates much as it did in Part I, where the Cooper (1986) curve dictates the number of crystals nucleated. One minor change was introduced such that ice does not initiate until the water vapor mixing ratio exceeds 25% supersaturation with respect to ice or water saturated and  $T < 260$  K.

Heterogeneous freezing of water drops directly follows Bigg (1953) and not the Wisner et al. (1972) interpretation of his work. Directly from Bigg (1953), the probability of certain volume drops freezing at specified temperatures is precomputed when the model starts and then stored in a lookup table using

$$P = 1 - \exp\{-120 \times \text{vol} \times 5.2 \times 10^{-4} \times [\exp(T - T_0) - 1]\}, \quad (\text{A12})$$

where  $P$  is the probability of freezing for water drops with volume (vol),  $T$  is air temperature, and  $T_0$  is the melting temperature (273.15 K).

The larger raindrops freeze into graupel whereas the smaller cloud droplets freeze into cloud ice. Homogeneous freezing of cloud water when  $T < -38^\circ\text{C}$  is implicitly handled by this technique, thereby eliminating the need for any explicit code to freeze water at lower temperatures.

Secondary ice particles are generated via the rime-splinter or Hallet–Mossop process in the same way they were detailed in Reisner et al. (1998). As in Part I, graupel must be present in the proper temperature range for the secondary process to occur.

### 4) GROWTH OF CLOUD ICE—CONVERSION TO SNOW

Cloud ice particles are nucleated with an arbitrary initial mass of  $10^{-12}$  kg ( $D \approx 4 \mu\text{m}$ ) and grow by vapor deposition only following Srivastava and Coen (1992). While cloud ice does follow the complete gamma dis-

tribution (with diameters from zero to  $\infty$ ), the fraction of ice mass with particle diameters greater than  $200 \mu\text{m}$  is immediately transferred to the snow category each time step. In place of rather complex alternatives like Harrington et al. (1995), a lookup table is precomputed from the mixing ratio, number concentration, and  $\mu_i$ , to determine the amount of ice with diameters greater than  $200 \mu\text{m}$  to convert to snow. Since cloud ice will regularly transfer to the snow category and therefore leave cloud ice as small crystals only, we neglect the riming process for cloud ice because Pruppacher and Klett (1997) indicate that smaller ice crystals do not accrete much cloud water.

### 5) DEPOSITION—SUBLIMATION OF ICE—SNOW—GRAUPEL

The process of vapor deposition onto snow and graupel (and the inverse process, sublimation) is treated nearly the same as rain evaporation following Srivastava and Coen (1992) except for the proper substitution of ice versus water substance. Ventilation coefficients, found in appendix B, follow Pruppacher and Klett (1997) and dimensionless capacitance values for snow linearly decrease from 0.5 (spherical value) to 0.3 as temperature increases from  $-30^\circ$  to  $-15^\circ\text{C}$ . As snow sublimates, it does not convert back into the cloud ice category, which should not be a problem since the snow distribution includes all diameters. Unlike the Reisner et al. (1998) scheme, the new scheme properly computes the sublimation of snow and graupel when temperatures exceed  $0^\circ\text{C}$ . This was previously neglected purely because of coding practices.

### 6) HYDROMETEOR COLLISION—COLLECTION

For hydrometeor collection (where species  $y$  collects species  $x$ ), an integral form of the collection equation is used following Verlinde et al. (1990):

$$\frac{dr_y}{dt} = \frac{\pi}{4} \int \int E_{xy} m(D_x) (D_x + D_y)^2 \times [v(D_x) - v(D_y)] N(D_x) N(D_y) dD_x dD_y. \quad (\text{A13})$$

Unlike many other BMPs, the collection efficiency  $E_{xy}$  varies as a function of the MVD of the collector–collected species and is not assumed to be constant.<sup>A1</sup>

<sup>A1</sup> For example, when rain collects cloud water, the efficiency is computed from each species' MVD following Beard and Grover (1974) for diameter ratios  $< 0.1$  and by curve fitting data shown in Pruppacher and Klett (1997, their Fig. 14-9) for larger diameter ratios. A lookup table is created at the start of a simulation.

Next, for a few processes, like rain, snow, and graupel collecting cloud water, Eq. (A13) is simplified to

$$\frac{dr_y}{dt} = \frac{\pi}{4} E_{xy} q_x \rho \int D_y^2 v(D_y) N(D_y) dD_y, \quad (\text{A14})$$

by applying the Wisner et al. (1972) approximation whereby  $D_y \gg D_x$  and  $v(D_y) \gg v(D_x)$ . After substitution, this can be rewritten as

$$\frac{dr_y}{dt} = \frac{\pi}{4} E_{xy} q_x \rho \int D_y^2 \left( \frac{\rho_0}{\rho} \right)^{1/2} \alpha D_y^\beta e^{-fD} N_{0,y} D_y^\mu e^{-\lambda D_y} dD_y, \quad (\text{A15})$$

then integrated to culminate in

$$\frac{dr_y}{dt} = \frac{\pi}{4} E_{xy} r_x \left( \frac{\rho_0}{\rho} \right)^{1/2} \alpha_y N_{0,y} \frac{\Gamma(\mu_y + \beta_y + 3)}{(\lambda + f_y)^{(\mu_y + \beta_y + 3)}}. \quad (\text{A16})$$

However, when the two interacting species have similar fall speeds, the full double integral is needed but rarely applied in current BMPs. For example, when rain collects graupel or snow, many BMPs continue to use the Wisner et al. (1972) simplification, yet Mizuno (1990) clearly showed its inaccuracies. While Mizuno (1990) proposed a substitute relation for the velocity difference term and Verlinde et al. (1990) offered an entirely new mathematical solution, both integrated for *all* diameters from zero to  $\infty$ . We argue that the upper limit of the inner integral should stop when the diameter of the collected species produces a terminal velocity that equals the terminal velocity of the collector species. Instead of making any simplifying assumptions, the new scheme uses the full double integral with the inner integration limits from zero to the aforementioned diameter. The calculations using Eq. (A13) for 100 logarithmically spaced diameter bins are performed when the WRF/MM5 starts and thereafter are stored for later application during each time step.

The hydrometeor collection process becomes complicated when the two species involved in collisions result in the creation of a third species. Such is the case when rain collects either cloud ice or snow (when  $T < 0^\circ\text{C}$ ) and results in graupel. Not only does the mass of the frozen species collected need to be summed using Eq. (A13), but the mass of the collector species needs to be summed into the new species as well. Therefore, when rain collects either frozen particle, the masses of both species are summed to find the production rate of graupel and each species loses their correct respective mass. In other BMPs (e.g., Reisner et al. 1998), only the collected species were transferred to the new species, which in the case of cloud ice was a nearly negligible amount compared to the mass of rain (collector species).

Finally, since the new scheme utilizes a lookup table generated from 100 size bins of rain and snow, we implemented another first in a bulk model that mimics what most explicit bin models do. In the case of rain-collecting snow (and its inverse), we traverse their size bins and if the mass of the water drop exceeds the mass of the snow particle, we assume the two particles join as one, thus freezing the drop into graupel (hail in reality) and removing the mass of each particle from their respective species. If, on the other hand, the water drop mass is less than the snow particle mass, the snow simply accretes the water drop, thus increasing snow mass and decreasing rain mass. This technique follows the bin models of Geresdi (1998) and Lynn et al. (2005).

## 7) CONVERSION OF RIMED SNOW TO GRAUPEL

One of the largest uncertainties in microphysical schemes relates to the treatment of graupel produced from rimed snow. Even explicit bin microphysical schemes use a variety of ad hoc methods to decide when to transfer rimed snow into a new hydrometeor category like graupel, yet those assumptions can greatly influence QPFs. Rutledge and Hobbs (1983) used threshold amounts of cloud water and snow before creating graupel. Murakami (1990) used a 1:1 ratio of riming to depositional growth as an initiation threshold. In our new scheme, we likewise compute this ratio. As it increases from 5:1 to 30:1, we linearly increase the production rate of graupel from 5% to 75% of the riming rate. The remainder of the riming rate (from 95% to 25%) simply becomes a snow production rate due to the collection of cloud water. All of these techniques are admittedly ad hoc and future research is sorely needed to mimic the real situation.

## 8) MELTING ICE, SNOW, AND GRAUPEL

Since cloud ice is so small, it is assumed to melt instantaneously at the first level where  $T > 0^\circ\text{C}$ . Snow and graupel melt gradually in thermodynamic equilibrium with the surrounding air. The melting process is unchanged from Reisner et al. (1998) except that the assumed distribution shape of each species is properly integrated. As was done in Rutledge and Hobbs (1983), the melting rates are increased when snow is actively collecting rain and/or cloud water.

## 9) SEDIMENTATION

The sedimentation process is relatively standard when compared with other BMPs. The mass-weighted mean terminal velocity of each species is computed following their respective distribution assumptions. These

are applied to the mass mixing ratios in the typical forward-in-time, backward-in-space technique. As mentioned previously, since cloud ice is a double-moment species, its number concentration properly sediments at its number-weighted mean terminal velocity.

There are two special cases for sedimentation that require more details. First, in order to compute the graupel produced from rimed snow, we stored the riming to depositional growth ratio. This ratio is further used to determine a snow terminal velocity “boosting factor” and applied to heavily rimed snow. Essentially, we desire that rimed snow fall slightly faster than unrimed snow as observations appear to indicate (Locatelli and Hobbs 1974). Using the same 5:1 to 30:1 ratio amounts, we linearly increase snow’s terminal velocity from 10% to 50% over that range.

The other special case for sedimentation treats melting snow and graupel. In classical single-moment BMPs, the snow and graupel mixing ratios significantly decrease below the melting level, thus causing their mass-weighted terminal velocities to decrease as well. Observations of natural snow melting, however, show that snow falls faster as it melts. Thus, for over two decades since Lin et al. (1983), the treatment of melting and falling snow and graupel has been backward from nature. In this new scheme, below the melting level, we use the maximum of the computed snow and rain terminal velocities applied to snow, and the maximum computed graupel and rain terminal velocities applied to graupel. Therefore, partially melted snow or graupel fall at the same speed as the coexisting rain below the melting level.

## APPENDIX B

### List of Symbols

TABLE B1. List of symbols found in the text.

Symbol	Value	Description
$a$	See Table A1	Mass power-law constant (varies for different species)
$b$	See Table A1	Mass power-law constant (varies for different species)
$C$	0.3, 0.5	Dimensionless capacitance (for vapor diffusional growth) for aggregates and spheres
$D$	Variable	Diameter of particle
$D_b$	See Eq. (A11)	Characteristic diameter of cloud droplet distribution computed from $D_g$ and $D_f$
$D_f$	See Eq. (A9)	Characteristic diameter (related to mean size) of cloud droplet distribution
$D_g$	See Eq. (A10)	Characteristic diameter (related to reflectivity) of cloud droplet distribution
$E_{xy}$	Variable	Collision efficiency of species $y$ collecting species $x$
$F$	Variable	Ventilation coefficient $F = 0.86 + 0.28S_c^{1/3}R_e^{1/2}$ for snow/graupel and $F = 0.78 + 0.308S_c^{1/3}R_e^{1/2}$ for rain
$f$	See Table A1	Velocity power-law constant (varies for different species)
$K_s$	Variable	Diffusivity of water vapor in air
$k_t$	Variable	Thermal conductivity of air
$L_s$	$2.834 \times 10^6$	Latent heat of sublimation
$\mathcal{M}_n$	See Eq. (2)	$n$ th moment of the snow size distribution
$m$	See Eq. (A2)	Mass
$N_c$	$100 \times 10^6$	Number concentration of cloud water droplets
$N_0$	See Eq. (A5)	Intercept parameter for exponential or gamma distribution
$N_{0,r}$	See Eq. (A6)	Variable intercept parameter for rain
$N_{0,g}$	See Eq. (A7)	Variable intercept parameter for graupel
$N_1$	$9 \times 10^9$	Constant used in Eq. (A6) for computing rain-variable intercept parameter
$N_2$	$2 \times 10^6$	Constant used in Eq. (A6) for computing rain-variable intercept parameter
$N_i$	See Eq. (A1)	Number concentration of a particular hydrometeor species
$q_{r0}$	$1 \times 10^{-4}$	Constant used in Eq. (A6) for computing rain-variable intercept parameter
$q_x$	Variable	Mass mixing ratio of species $x$
$R_e$	Variable	Reynolds number, $R_e = v(D)D\rho/\nu$
$R_v$	461.5	Gas constant for water vapor
$r_x$	Variable	Mass water content of species $x$
$r_{si}$	Variable	Saturation mixing ratio over ice
$S_c$	0.632	Schmidt number
$S_i$	Variable	Saturation with respect to ice
$v$	See Eq. (A3)	Velocity
$\alpha$	See Table A1	Velocity power-law constant (varies for different species)
$\beta$	See Table A1	Velocity power-law constant (varies for different species)
$\kappa_0$	490.6	Snow size distribution constant [see Eq. (1)]

TABLE B1. (Continued)

Symbol	Value	Description
$\kappa_1$	17.46	Snow size distribution constant [see Eq. (1)]
$\Lambda_0$	20.78	Snow size distribution constant [see Eq. (1)]
$\Lambda_1$	3.29	Snow size distribution constant [see Eq. (1)]
$\lambda$	Variable	Gamma size distribution slope parameter
$\mu$	See Table A1	Gamma size distribution shape parameter (varies for different species)
$\rho$	Variable	Moist air density
$\rho_0$	1.185	Reference air density
$\nu$	Variable	Dynamic viscosity of air

## APPENDIX C

and

**Detailed Calculation of Vapor Depositional Growth of Snow**

From Srivastava and Coen (1992), the depositional growth of a single particle is calculated using

$$\frac{dm}{dt} = \frac{2\pi D F K_s r_{si} S_i}{1 + \gamma} (1 - \alpha S_i + \alpha^2 S_i^2 - 5\alpha^3 S_i^3), \quad (C1)$$

where

$$\alpha = \frac{1}{2} \left( \frac{\gamma}{1 + \gamma} \right)^2 \frac{r_{si}'' r_{si}}{r_{si}' r_{si}'}, \quad (C2)$$

$$\gamma = \frac{L_s K_s r_{si}'}{k_t}, \quad (C3)$$

$$r_{si}' = \frac{r_{si}}{T} \left( \frac{L_s}{R_v T} - 1 \right), \quad (C4)$$

$$r_{si}'' = r_{si} \left\{ \left[ \frac{1}{T} \left( \frac{L_s}{R_v T} - 1 \right) \right]^2 - 2 \frac{L_s}{R_v T^3} + \frac{1}{T^2} \right\}, \quad (C5)$$

with the parenthesized term in Eq. (C1) as their correction factor. Then, integrating for particles of all diameters and collapsing all variables that do not have a diameter dependence into  $C_1$ , thus leaving only  $D$  and  $F$  within the integral, leads to

$$\frac{dq_s}{dt} = C_1 \int_0^\infty D F N(D) dD. \quad (C6)$$

Next, expansion of the ventilation coefficient and its associated velocity–diameter relationship [Eq. (A3)] reveals the final integral to be

$$\frac{dq_s}{dt} = 0.86 C_1 \int_0^\infty D N(D) dD + 0.28 S_c^{1/3} \left( \frac{\rho}{\nu} \right)^{1/2} \left( \frac{\rho_0}{\rho} \right)^{1/2} \alpha_s^{1/2} C_1 \int_0^\infty D \left( \frac{\beta_s + 1}{2} + 1 \right) N(D) dD. \quad (C7)$$

Finally, Eq. (2) representing moments  $\mathcal{M}$  of the PSD can be substituted for the two integrals on the right-hand side to yield

$$\frac{dq_s}{dt} = 0.86 C_1 \mathcal{M}_1 + 0.28 S_c^{1/3} \left( \frac{\rho}{\nu} \right)^{1/2} \left( \frac{\rho_0}{\rho} \right)^{1/2} \alpha_s^{1/2} C_1 \mathcal{M} \left( \frac{\beta_s + 1}{2} + 1 \right). \quad (C8)$$

The next step utilizes the model-predicted snow content and temperature while applying the Field et al. (2005) power-law relationship between moments of the PSD,

$$\mathcal{M}_n = a(n, T_c) \mathcal{M}_2^{b(n, T_c)}, \quad (C9)$$

and associated constants (given in their Table 2 and repeated below):

$$\begin{aligned} \log a(n, T_c) = & 5.065\,339 - 0.062\,659 T_c - 3.032\,362 n \\ & + 0.029\,469 T_c n - 0.000\,285 T_c^2 \\ & + 0.312\,550 n^2 + 0.000\,204 T_c^2 n \\ & + 0.003\,199 T_c n^2 + 0.000\,000 T_c^3 \\ & - 0.015\,952 n^3 \quad \text{and} \end{aligned} \quad (C10)$$

$$\begin{aligned}
b(n, T_c) = & 0.476\,221 - 0.015\,896T_c + 0.165\,977n \\
& + 0.007\,468T_cn - 0.000\,141T_c^2 + 0.060\,366n^2 \\
& + 0.000\,079T_c^2n + 0.000\,594T_cn^2 \\
& + 0.000\,000T_c^3 - 0.003\,577n^3, \quad (C11)
\end{aligned}$$

where  $n$  is the moment order and  $T_c$  is air temperature in degrees Celsius.

In practice, Eq. (C9) requires a standard or reference moment (from which the given constants to convert to other moments were originally computed), in this case, the second moment. Since our mass–diameter relation uses the exponent value  $b_s = 2$ , the second moment is simply snow content divided by the prefactor,  $a_s$ . If a different value for the exponent were used, then the second moment,  $M_2$ , must be precomputed before computing any other moments. Therefore, to solve Eq. (C8), thereby arriving at the final value for depositional growth of snow (or its inverse, sublimation), we compute  $M_1$  and  $M_{[(\beta_s+1)/2+1]}$  using Eq. (C9) and the model inputs of temperature and snow content.

#### REFERENCES

- Beard, K. V., and S. N. Grover, 1974: Numerical collision efficiencies for small raindrops colliding with micron size particles. *J. Atmos. Sci.*, **31**, 543–550.
- Berry, E. X., and R. L. Reinhardt, 1974: An analysis of cloud droplet growth by collection. Part II: Single initial distributions. *J. Atmos. Sci.*, **31**, 2127–2135.
- Bigg, E. K., 1953: The supercooling of water. *Proc. Phys. Soc. London*, **B66**, 688–694.
- Brandes, E. A., K. Ikeda, G. Zhang, M. Schonhuber, and R. M. Rasmussen, 2007: A statistical and physical description of hydrometeor distributions in Colorado snowstorms using a video disdrometer. *J. Appl. Meteor. Climatol.*, **46**, 634–650.
- Braun, S. A., and W.-K. Tao, 2000: Sensitivity of high-resolution simulations of Hurricane Bob (1991) to planetary boundary layer parameterizations. *Mon. Wea. Rev.*, **128**, 3941–3961.
- Cooper, W. A., 1986: Ice initiation in natural clouds. *Precipitation Enhancement—A Scientific Challenge*, Meteor. Monogr., No. 43, Amer. Meteor. Soc., 29–32.
- Cox, G. P., 1988: Modelling precipitation in frontal rainbands. *Quart. J. Roy. Meteor. Soc.*, **114**, 115–127.
- Doherty, A. M., T. R. Sreerekha, U. M. O’Keeffe, and S. J. English, 2007: Ice hydrometeor assumptions in radiative transfer models at AMSU-B frequencies. *Quart. J. Roy. Meteor. Soc.*, **133**, 1205–1212.
- Evans, A. G., J. D. Locatelli, M. T. Stoelinga, and P. V. Hobbs, 2005: The IMPROVE-1 storm of 12 February 2001. Part II: Cloud structures and the growth of precipitation. *J. Atmos. Sci.*, **62**, 3456–3473.
- Fabry, F., and W. Szyrmer, 1999: Modeling of the melting layer. Part II: Electromagnetic. *J. Atmos. Sci.*, **56**, 3593–3600.
- Ferrier, B. S., 1994: A double-moment multiple-phase four-class bulk ice scheme. Part I: Description. *J. Atmos. Sci.*, **51**, 249–280.
- Field, P. R., R. J. Hogan, P. R. A. Brown, A. J. Illingworth, T. W. Choulaton, and R. J. Cotton, 2005: Parameterization of ice-particle size distributions for mid-latitude stratiform cloud. *Quart. J. Roy. Meteor. Soc.*, **131**, 1997–2017.
- Flatau, P. J., R. L. Walko, and W. R. Cotton, 1992: Polynomial fits to saturation vapor pressure. *J. Appl. Meteor.*, **31**, 1507–1513.
- Geresdi, I., 1998: Idealized simulation of the Colorado hailstorm case: Comparison of bulk and detailed microphysics. *Atmos. Res.*, **45**, 237–252.
- Gilmore, M. S., and J. M. Straka, 2008: The Berry and Reinhardt autoconversion parameterization: A digest. *J. Appl. Meteor. Climatol.*, **47**, 375–396.
- , —, and E. N. Rasmussen, 2004: Precipitation uncertainty due to variations in precipitation particle parameters within a simple microphysics scheme. *Mon. Wea. Rev.*, **132**, 2610–2627.
- Harrington, J. Y., M. P. Meyers, R. L. Walko, and W. R. Cotton, 1995: Parameterization of ice crystal conversion process due to vapor deposition for mesoscale models using double-moment basis functions. Part I: Basic formulation and parcel model results. *J. Atmos. Sci.*, **52**, 4344–4366.
- Heymsfield, A. J., and M. Kajikawa, 1987: An improved approach to calculating terminal velocities of plate-like crystals and graupel. *J. Atmos. Sci.*, **44**, 1088–1099.
- , A. Bansemer, C. Schmitt, C. Twohy, and M. R. Poellot, 2004: Effective ice particle densities derived from aircraft data. *J. Atmos. Sci.*, **61**, 982–1003.
- , G.-J. van Zadelhoff, D. P. Donovan, F. Fabry, R. J. Hogan, and A. J. Illingworth, 2007: Refinements to ice particle mass dimensional and terminal velocity relationships for ice clouds. Part II: Evaluation and parameterizations of ensemble ice particle sedimentation velocities. *J. Atmos. Sci.*, **64**, 1068–1088.
- Holroyd, E. W., III, 1971: The meso- and microscale structure of Great Lakes snowstorm bands: A synthesis of ground measurements, radar data, and satellite observations. Ph.D. dissertation, University at Albany, State University of New York, 148 pp.
- Hong, S.-Y., J. Dudhia, and S.-H. Chen, 2004: A revised approach to ice microphysical processes for the bulk parameterization of clouds and precipitation. *Mon. Wea. Rev.*, **132**, 103–120.
- Houze, R. A., P. V. Hobbs, P. H. Herzegh, and D. B. Parsons, 1979: Size distributions of precipitation particles in frontal clouds. *J. Atmos. Sci.*, **36**, 156–162.
- Khairoutdinov, M., and Y. Kogan, 2000: A new cloud physics parameterization in a large-eddy simulation model of marine stratocumulus. *Mon. Wea. Rev.*, **128**, 229–243.
- Kim, M. J., M. S. Kulie, C. O’Dell, and R. Bennartz, 2007: Scattering of ice particles at microwave frequencies: A physically based parameterization. *J. Appl. Meteor. Climatol.*, **46**, 615–633.
- Langlois, W. E., 1973: A rapidly convergent procedure for computing large-scale condensation in a dynamical weather model. *Tellus*, **25**, 86–87.
- Lin, Y. L., R. Farley, and H. D. Orville, 1983: Bulk parameterization of the snow field in a cloud model. *J. Climate Appl. Meteor.*, **22**, 1065–1092.
- Locatelli, J. D., and P. V. Hobbs, 1974: Fall speeds and masses of solid precipitation particles. *J. Geophys. Res.*, **79**, 2185–2197.
- , M. T. Stoelinga, M. F. Garvert, and P. V. Hobbs, 2005: The IMPROVE-1 storm of 1–2 February 2001. Part I: Development of a forward-tilted cold front and warm occlusion. *J. Atmos. Sci.*, **62**, 3431–3455.
- Lynn, B. H., A. P. Khain, J. Dudhia, and A. Seifert, 2005: Spectral

- (bin) microphysics couple with a mesoscale model (MM5). Part II: Simulation of a CaPE rain event with a squall line. *Mon. Wea. Rev.*, **133**, 59–71.
- Magano, C., and T. Nakamura, 1965: Aerodynamic studies of falling snowflakes. *J. Meteor. Soc. Japan*, **43**, 139–147.
- Martin, G. M., D. W. Johnson, and A. Spice, 1994: The measurement and parameterization of effective radius of droplets in warm stratocumulus clouds. *J. Atmos. Sci.*, **51**, 1823–1842.
- Meyers, M. P., R. L. Walko, J. Y. Harrington, and W. R. Cotton, 1997: New RAMS cloud micro-physics parameterization. Part II: The two-moment scheme. *Atmos. Res.*, **45**, 3–39.
- Milbrandt, J. A., and M. K. Yau, 2005: A multimoment bulk microphysics parameterization. Part I: Analysis of the role of the spectral shape parameter. *J. Atmos. Sci.*, **62**, 3051–3064.
- Mitchell, D. L., and A. J. Heymsfield, 2005: Refinements in the treatment of ice particle terminal velocities, highlighting aggregates. *J. Atmos. Sci.*, **62**, 1637–1644.
- , R. Zhang, and R. L. Pitter, 1990: Mass-dimensional relationships for ice particles and the influence of riming on snowfall rates. *J. Appl. Meteor.*, **29**, 153–163.
- Mizuno, H., 1990: Parameterization of the accretion process between different precipitation elements. *J. Meteor. Soc. Japan*, **68**, 395–398.
- Morrison, H., and J. O. Pinto, 2005: Mesoscale modeling of springtime arctic mixed-phase stratiform clouds using a new two-moment bulk microphysics scheme. *J. Atmos. Sci.*, **62**, 3683–3704.
- Murakami, M., 1990: Numerical modeling of dynamical and microphysical evolution of an isolated convective cloud—The 19 July 1981 CCOPE cloud. *J. Meteor. Soc. Japan*, **68**, 107–128.
- Muramoto, K.-I., K. Matsuura, and T. Shiina, 1995: Measuring the density of snow particles and snowfall rate. *Electron. Commun. Japan*, **78**, 71–79.
- Pruppacher, H. R., and J. D. Klett, 1997: *Microphysics of Clouds and Precipitation*. D. Reidel, 714 pp.
- Reisner, J., R. M. Rasmussen, and R. T. Bruintjes, 1998: Explicit forecasting of supercooled liquid water in winter storms using the MM5 mesoscale model. *Quart. J. Roy. Meteor. Soc.*, **124**, 1071–1107.
- Rutledge, S. A., and P. V. Hobbs, 1983: The mesoscale and microscale structure and organization of clouds and precipitation in mid-latitude cyclones. XII: A diagnostic modeling study of precipitation development in narrow cold-frontal rainbands. *J. Atmos. Sci.*, **41**, 2949–2972.
- Seifert, A., and K. D. Beheng, 2006: A two-moment cloud microphysics parameterization for mixed-phase clouds. Part 1: Model description. *Meteor. Atmos. Phys.*, **92**, 45–66.
- Sekhon, R. S., and R. C. Srivastava, 1970: Snow spectra and radar reflectivity. *J. Atmos. Sci.*, **27**, 299–307.
- Srivastava, R. C., and J. L. Coen, 1992: New explicit equations for the accurate calculation of the growth and evaporation of hydrometeors by the diffusion of water vapor. *J. Atmos. Sci.*, **49**, 1643–1651.
- Stoelinga, M. T., and Coauthors, 2003: Improvement of microphysical parameterization through observational verification experiment. *Bull. Amer. Meteor. Soc.*, **84**, 1807–1826.
- Thompson, G., R. M. Rasmussen, and K. Manning, 2004: Explicit forecasts of winter precipitation using an improved bulk microphysics scheme. Part I: Description and sensitivity analysis. *Mon. Wea. Rev.*, **132**, 519–542.
- Verlinde, J., P. J. Flatau, and W. R. Cotton, 1990: Analytical solutions to the collection growth equation: Comparison with approximate methods and application to the cloud microphysics parameterization schemes. *J. Atmos. Sci.*, **47**, 2871–2880.
- Walko, R. L., W. R. Cotton, M. P. Meyers, and J. Y. Harrington, 1995: New RAMS cloud microphysics parameterization. Part I: The single-moment scheme. *Atmos. Res.*, **38**, 29–62.
- Wang, P. K., and W. Ji, 2000: Collision efficiencies of ice crystals at low-intermediate Reynolds numbers colliding with supercooled cloud droplets: A numerical study. *J. Atmos. Sci.*, **57**, 1001–1009.
- Westbrook, C. D., R. C. Ball, P. R. Field, and A. J. Heymsfield, 2004: Universality in snowflake aggregation. *Geophys. Res. Lett.*, **31**, L15104, doi:10.1029/2004GL020363.
- Wisner, C., H. D. Orville, and C. Myers, 1972: A numerical model of a hail-bearing cloud. *J. Atmos. Sci.*, **29**, 1160–1181.
- Woods, C. P., M. T. Stoelinga, and J. D. Locatelli, 2007: The IMPROVE-1 storm of 1–2 February 2001. Part III: Sensitivity of a mesoscale model simulation to the representation of snow particle types and testing of a bulk microphysical scheme with snow habit prediction. *J. Atmos. Sci.*, **64**, 3927–3948.